Characterization of X80 and X100 Microalloyed Pipeline Steel Using Quantitative X-ray Diffraction

J.B. WISKEL, X. LI, D.G. IVEY, and H. HENEIN

Quantitative X-ray diffraction characterization of four (4) X80 and three (3) X100 microalloyed steels was undertaken. The effect of through-thickness position, processing parameters, and composition on the measured crystallite size, microstrain, and *J* index (relative magnitude of crystallographic texture) was determined. Microstructure analysis using optical microscopy, scanning electron microscopy, transmission electron microscopy, and electron-backscattered diffraction was also undertaken. The measured value of microstrain increased with increasing alloy content and decreasing cooling interrupt temperature. Microstructural features corresponding to crystallite size in the X80 steels were both above and below the detection limit for quantitative X-ray diffraction. The X100 steels consistently exhibited microstructure features below the crystallite size detection limit. The yield stress of each steel increased with increasing microstrain. The increase in microstrain from X80 to X100 is also associated with a change in microstructure from predominantly polygonal ferrite to bainitic ferrite.

https://doi.org/10.1007/s11663-018-1298-4

I. INTRODUCTION

MICROSTRUCTURAL characterization of a microalloyed pipeline steel can take many forms,[1–10] including optical microscopy (OM), scanning electron microscopy (SEM), transmission electron microscopy (TEM), and electron-backscattered diffraction (EBSD). Due to the complexity of the microstructure inherent in microalloyed steels, most, if not all, of these techniques are used in a complimentary way to characterize this material.

Microstructural features in microalloyed steels can include the presence of several co-existing complex phases (*e.g.*, ferrite, acicular ferrite, or bainite),[3,4,11,12] dislocation density variations associated with the different phases,[4,13] preferred orientation,[10] and variations in grain size and/or subgrain size.[3] These microstructural features are directly related to the composition of the steel[5–8,13] and to the thermomechanical controlled processing (TMCP) conditions employed, including finish rolling temperature (FRT) and coiling interrupt temperature (CIT),[3,4] and ultimately with the mechanical properties of the material.[14]

Previous work by the authors[15] used quantitative X-ray diffraction (QXRD) to quantify the mean size and atomic composition of nanosize precipitates in microalloyed steels. This paper focuses on applying the general QXRD technique to the characterization of microstructure, specifically crystallite size (D_v), microstrain (ε_o), and texture index (J), for four (4) X80 and three (3) X100 microalloyed pipeline steels. These specific QXRD microstructure features are related to grain/subgrain size, dislocation density and texture, respectively.

The measured QXRD values of crystallite size (D_v), microstrain (ε_o), and texture index (J) are correlated with CIT, FRT, composition, and both yield strength (σ_y) and the yield strength-to-tensile strength ratio (Y/TS). OM, SEM, TEM, and EBSD analysis of the steel microstructures was also undertaken to assess the crystallite size measurements obtained in the analysis. The use of QXRD as a complementary characterization technique for microalloyed steels is assessed.

II. BACKGROUND

Quantitative X-ray diffraction (QXRD) is an indirect microstructure characterization technique that is used in this contribution to quantify crystallite size, microstrain, and the relative magnitude of preferred orientation (*via* a *J* index term) in a crystalline material. This section will briefly describe the basics of QXRD and then review the concepts associated with crystallite size, microstrain, and preferred orientation.

J.B. WISKEL, X. LI, D.G. IVEY, and H. HENEIN are with the Department of Chemical and Materials Engineering, University of Alberta, Edmonton, AB, T6G 1H9, Canada. Contact e-mail: bwiskel@ualberta.ca.

Manuscript submitted January 29, 2018.
Article published online June 4, 2018.

A. *Quantitative X-ray Diffraction (QXRD)*

QXRD entails mathematically calculating an X-ray diffraction pattern (*i.e.*, intensity *vs* the 2θ scattering angle) for a material from first principles.[15] The variables used in the calculation include fundamental crystallographic parameters, such as unit cell type and size, atom type and instrument parameters, and material characteristics like diffraction crystallite (domain) size, microstrain, and preferred orientation.

A number of QXRD programs (*e.g.*, GSAS, TOPAS) are widely available. The program used in this study is TOPAS Academic Software 4.1 (Bruker AXS Inc., Madison, WI, 2007). This program uses a fundamental parameter approach[16,17] in calculating a diffraction pattern. In addition, TOPAS incorporates the effect of crystallite size, microstrain, and preferred orientation in the diffraction pattern calculation.

B. *Crystallite Size*

Crystallite size (D_v) is a measurement of the depth (perpendicular to the diffraction plane) of a continuous set of coherent planes that contribute to Bragg diffraction. However, for ease of usage, the term crystallite size will be used. In materials with relatively large crystallite sizes, the diffraction peak decays rapidly on either side of the Bragg angle due to destructive wave interference of X-rays scattered from the near-surface plane of atoms and those scattered from a relatively distant plane (depth wise) in the material. The net result is a relatively narrow diffraction peak.

However, as crystallite size (*i.e.*, depth of a continuous set of planes) decreases below approximately 200 nm,[18] the diffraction peak begins to broaden due to incomplete annihilation of the diffracted X-rays at diffraction angles on either side of the Bragg peak. This incomplete wave annihilation results in a measureable broadening of the diffraction peak (beyond any intrinsic instrumental broadening) and can be related to the physical size (*i.e.*, depth) of the continuous set of planes. This set of planes is analogous to either grain size for homogeneous microstructures or subgrain/dislocation cell size in microstructures exhibiting dislocation substructures. Both X80 and X100 microalloyed steels fall into the second grouping.

Broadening of the XRD peak due to crystallite size depends not only on the dimension normal to the diffracting planes, but also on the geometric shape[19] of the diffracting planes in three dimensions (*e.g.*, cubes *vs* spheres).[20] As a further complication, there is usually not a single specific crystallite size, but a distribution of sizes that can complicate the broadening effect, hence, the use of an average crystallite size value D_v.

In the context of microalloyed steels, both high-angle grain boundaries (HAGB) and dislocation substructures (*i.e.*, subgrains) can be present. A number of studies[3,4,6,12,21,22] have been conducted on the measurement of grain size in TMCP microalloyed steels. Optical microscopy, SEM, and/or EBSD have been used to directly measure grain size (defined HAGB) in these steels. The grains are typically greater than 1 μm in size—well beyond the resolution capacities of QXRD. However, with the evolution of TMCP processing aimed at decreasing grain size and/or producing different phase(s) (*e.g.*, bainitic structures), the interior of an individual grain may consist of dislocation substructures (*e.g.*, subgrains and/or dislocation cells) which are significantly finer in size.[4,6] These fine scale substructures may be amenable to characterization using QXRD.

A number of studies have been conducted using QXRD to characterize the crystallite size (and microstrain) of pure copper,[23] nickel coatings,[24] stainless steel,[25] and milled iron.[26] The measured value of D_v in these studies ranged from 20 to 160 nm. Dalla Torre *et al.*[23] compared the subgrain sizes derived from EBSD (based on a 2 deg misorientation angle) and TEM analysis with the D_v value obtained from QXRD for copper samples subjected to large deformations. The subgrain sizes (after 12 deformation passes) measured using EBSD and TEM were 130 ± 80 and 165 ± 90 nm, respectively. The crystallite size (D_v) calculated using QXRD was 63 nm. This study indicated that QXRD crystallite size can provide complimentary information on the internal substructure present in the microstructure on a scale comparable to both EBSD and TEM measurements for microalloyed steels.

C. *Microstrain*

Microstrain arises from local atomic positional distortions in the crystal lattice due to the presence of defects such as dislocations, solid solution elements, and vacancies. These local distortions manifest themselves as a broadening of the diffraction peak due to subtle changes in the lattice parameter. As the number of defects/inhomogeneities in the material increases (*e.g.*, higher dislocation density), the microstrain within the crystallite increases and, hence, peak broadening increases.

Dislocation density can be measured directly by TEM (by counting dislocations) and indirectly by EBSD. For QXRD, dislocation density can be calculated from the microstrain and crystallite size, using the Williamson and Smallman approach.[27] This approach assumes a uniform distribution of dislocations. However, dislocations in a material can exist at varying densities between the interior of the crystallite and near grain/subgrain boundaries that may result in non-symmetrical diffraction peak broadening.[28] In this work, a mean microstrain value (ε_o) is determined to characterize the average peak broadening due to microstrain.

Several studies have used the microstrain value from QXRD to measure a material's response to plastic deformation[23,27,28] and/or heat treatment.[29] In the former studies, microstrain was observed to increase with increased amount of plastic deformation (*i.e.*, cold work). A direct measurement of dislocation density was not undertaken. In the heat treatment study, dislocation density was calculated from a Williamson–Hall plot and was observed to vary with annealing temperature. The variation in microstrain was associated with various

metallurgical phenomena (*e.g.*, phase transformation, recovery) that occur at different heat treatment temperatures. A direct measurement of the dislocation density was not undertaken in the study.

Given the unknowns associated with both dislocation location and density variation (discussed above) and also a lack of direct validation of QXRD measured dislocation density for microalloyed steels, for the purpose of this work, only the mean microstrain value (ε_o) is considered (*i.e.*, a specific dislocation density value will not be calculated).

As both crystallite size and microstrain result in broadening of the diffraction peak, their individual effects are separated by the use of appropriate profile functions where microstrain is loosely associated with a Gaussian function and size broadening with a Lorentzian function.[15] The application of both the Lorentzian and Gaussian functions into the diffraction calculations is based on the experimental usefulness of both functions in describing peak broadening and not a fundamental first principles relationship with either crystallite size or microstrain.

D. *Preferred Orientation*

A third microstructure feature observed in the diffraction patterns of deformed (*e.g.*, rolled) crystalline metals is the preferred orientation of specific crystallographic planes parallel to the rolling surface.[10] The General Spherical Harmonics (GSH) model is used in TOPAS and applies a shaping function that alters the intensity of the diffraction peaks relative to a non-textured distribution of grains. To quantify the magnitude of the crystalline texture (*i.e.*, how much the shaping functions alter the peak intensities), a J index[30] is calculated as per the following equation:

$$J = 1 + \sum_{l=2}^{L} \left(\frac{1}{2l+1} \right) \sum_{m=-l}^{l} \sum_{n=-l}^{l} \left| C_l^{mn} \right|^2, \qquad [1]$$

where C_l^{mn} are the spherical harmonic parameters obtained from QXRD analysis where L is the number of terms in the spherical harmonic equation. A value of $J = 1$ indicates a completely random (non-textured) structure. As the value of J increases above 1, the magnitude of preferred orientation in the microstructure also increases.[30]

III. MATERIALS AND METHODS

This section will detail the composition, tensile properties, and processing parameters of the X80 and X100 steels analyzed in this work. X80 and X100 are pipeline steels exhibiting a specific minimum yield stress (SMYS) of 80 ksi (550 MPa) and 100 ksi (689 MPa), respectively. In addition, sample location and preparation, X-ray diffraction testing, and microstructure analysis using OM, SEM, TEM, and EBSD are described.

A. *Steels Analyzed*

The thickness, composition, processing conditions, and mechanical properties for the X80 and X100 steels analyzed in this work are presented in Table I. The values of the finish rolling temperature (FRT) and coiling interrupt temperature (CIT) have been normalized to the X100-2B temperature values for each of these processing variables. The FRT is relatively constant for the steels tested except for X80-462 and X80-A4B, which were processed with slightly lower and higher FRT, respectively.

Conversely, there is a much wider range of CIT values, with the X100 steels exhibiting lower CIT values and the X80 steels higher CIT values. In addition, the combined Ni + Mo + Mn composition is higher for the X100 steels. Included in Table I are the yield strengths (σ_y) and tensile strengths (TS) obtained from 10.2-mm-diameter circular cross-section tensile specimens.

B. *XRD Sample Location and Preparation*

Rectangular slices (1 cm × 1 cm × 1 mm in thickness) were obtained from different through-thickness locations (*e.g.*, top surface, centerline, bottom surface) from either spiral pipe (X80) or plate (X100) for XRD analysis. The pipe samples were obtained from a 90 deg position with the spiral weld at the 0 deg position. The inner diameter of the X80 pipe samples is given a reference location of 0, which corresponds to the top surface of the skelp originally used to make the pipe. The 0 reference location for the X100 plate corresponds to the top surface of the plate. A reference location of 1 corresponds to the bottom of the skelp. An example of an XRD sample taken at the surface position (0) is

Table I. Composition, Properties, and Processing of Steels Analyzed

Heat #	t (mm)	C (Wt Pct)	Ni + Mo + Mn (Wt Pct)	FRT*	CIT*	σ_y (MPa)	TS (MPa)
X80-462	11.8	0.03	2.24	0.94	1.47	588	703
X80-A4B	12.1	0.04	2.26	1.05	1.32	568	694
X80-A4F	15.6	0.05	2.58	1.00	1.28	589	717
X80-B4F	15.1	0.05	2.33	1.00	1.42	592	735
X100-2A	14.4	0.04	2.69	1.00	1.00	810	907
X100-2B	14.0	0.07	2.71	1.00	0.90	691	793
X100-3C	14.6	0.06	2.68	1.00	1.14	744	846

*Normalized to the value for X100-2B steel.

shown in Figure 1. The XRD sample (defined by the dashed line sectioning cut) is oriented with the surface of the section parallel to the L-T rolling plane.

After sectioning, the L-T face was ground, mechanically polished, and then electrolytically polished[2] to remove the effect of polishing surface work hardening. Electropolishing was undertaken at room temperature in a 1 pct tetramethylammonium chloride, 10 pct acetylacetone, and methanol solution at a current of 4 mA. An electro polishing time of 16 hours removes approximately 50 μm of material from each section surface.

C. *X-ray Diffraction Testing*

XRD patterns were obtained using a Rigaku Geigerflex Powder Diffractometer with a Co target. Scanning angles (2θ) ranged from 40 to 125 deg for the steel samples and 20 to 125 deg for the LaB_6 standard. A step size of 0.02 deg was used with a counting time of 0.6 s. Instrument parameters include a receiving slit = 0.6 mm and a divergent slit angle = 1 deg. A LaB_6 standard was tested periodically to quantify instrument broadening (for inclusion in the QXRD analysis). The diffraction patterns were analyzed using TOPAS (described earlier) to determine the microstructural parameters D_v, ε_o, and J index.

D. *Microscopy*

Microstructure analysis of the steels was undertaken using OM, SEM, and TEM for X80-462 and X100-2A steels and EBSD for X80-462 steel only. Samples for optical microscopy and SEM were obtained from both near the surface (0) and centerline (0.5) regions. SEM analysis was carried out using a Hitachi S-2700 SEM, operated at a voltage of 20 kV and a working distance of 17 mm. A JEOL 2010 TEM operated at 200 kV was used to obtain bright field (BF) images for both X100-2A and X80-462 steels. TEM samples were obtained from a near-surface location corresponding to the normalized position (0). The EBSD portion of the study was conducted for the X80-462 steel at the surface (0), centerline (0.5), and bottom (1) positions using a JEOL 7000F SEM. The grid step size was 25 nm, the beam voltage was 25 kV, the working distance was 15 mm, and the sample was tilted to 70 deg. The pattern was automatically analyzed using the Channel 5 Flamenco software from HKL Technology.

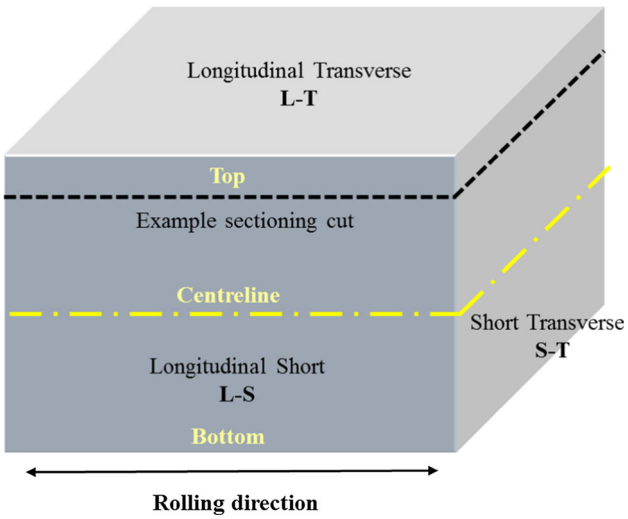

Fig. 1—Example of a sectioning cut of an XRD sample from the 0 position.

IV. RESULTS

A. *XRD Pattern for X100-2A (0.5)*

The measured XRD pattern obtained from the centerline position of X-100-2A (0.5) steel is shown in Figure 2. Included in this figure are labels indicating the Miller Indices ((110), (200), (211), and (220)) for each of the Bragg diffraction peaks for alpha iron. For an entirely random sample, the ratio of $I_{(110)}/I_{(211)}$ is 3.33. However, for the pattern shown in Figure 2, the $I_{(110)}/I_{(211)}$ ratio is 0.62 which indicates some degree of preferred orientation exists in the steel at the centerline location. The magnitude of preferred orientation, for this and all subsequent samples, is quantified using the J index parameter.

B. *QXRD*

For all the XRD patterns, a sequential whole profile fitting procedure was applied using TOPAS. The procedure includes the effect of instrument broadening (ascertained from a LaB_6 standard), refinement of the ferrite lattice parameter to align the diffraction peaks, background fitting, and then a systematic inclusion of crystallite size, microstrain, and the spherical harmonics function.

Figure 3(a) compares (magnified view) the measured (110) diffraction peak for X100-2A steel at the centerline (0.5) with the predicted XRD (110) profile that did not include the effect of either crystallite size (D_v) or microstrain (ε_o). An appreciable difference between the measured and predicted (110) peak profiles is observed. The difference in broadening between the two diffraction patterns is assessed using the difference in the full width half-maximum (ΔFWHM) for each peak. For the (110) peaks shown in Figure 3(a), a value of ΔFWHM = 0.177 deg was determined. The inclusion of both crystallite size and microstrain effects into the QXRD calculations results in a relatively good fit between the observed and predicted profiles for the (110) peak (Figure 3(b)).

The predicted microstructure values for X100-2A steel (0.5) are as follows: crystallite size (D_v) = 40 nm, microstrain (ε_o) = 12.6 pct, and J index = 1.27. The weighted residual error (R_{wp}) used to assess the "fit" between the predicted pattern (Y_{QXRD}) and the measured pattern (Y_m) is 22.1. The lower the value of R_{wp}, the better the fit between the measured and predicted

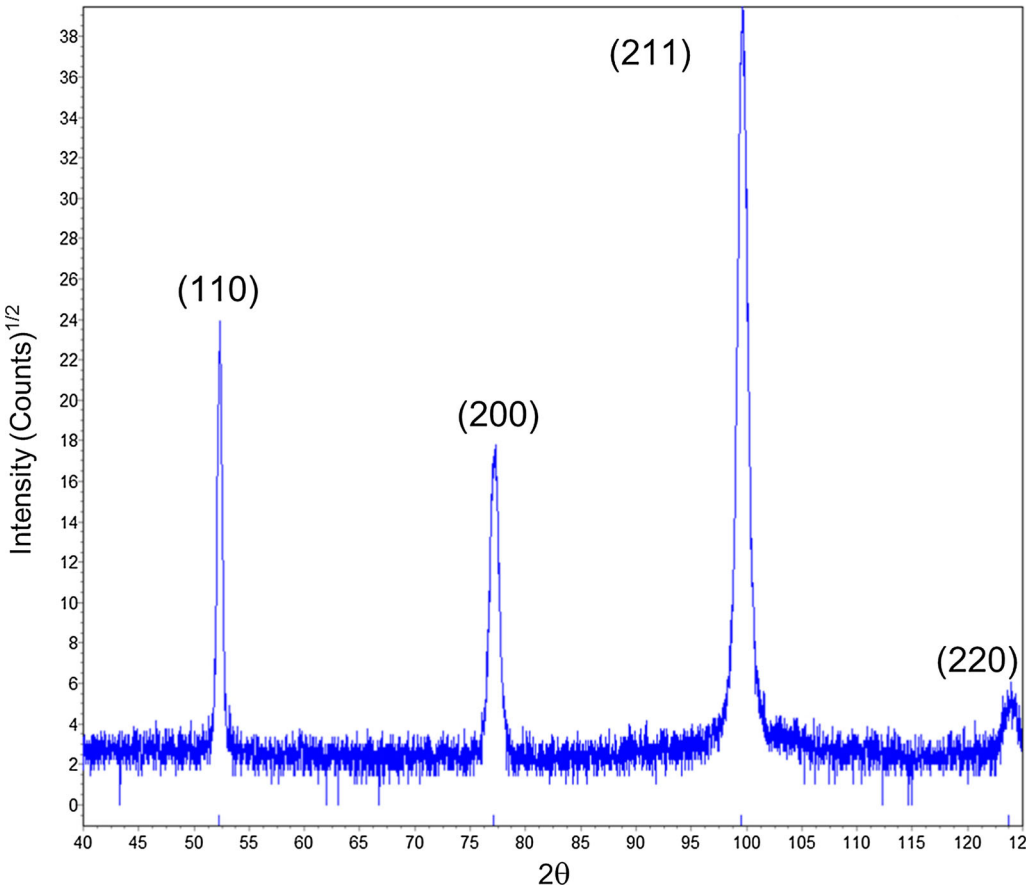

Fig. 2—XRD pattern for X100-2A steel at the centerline position (0.5).

patterns. The predicted microstructure values for all the steel samples tested are tabulated in Table II for the X80 steels and in Table III for the X100 steels. Included in these tables are the relative positions of the XRD samples, D_v, ε_o, J index, the $(I_{(110)}/I_{(211)}$ ratio, R_{wp}, and ΔFWHM for the (110) peak. A value of 4500 nm for crystallite size indicates a crystallite size greater than the sensitivity of QXRD. This sensitivity will be discussed in detail in Section V.

C. *OM and SEM Microstructure Analysis*

Microstructure analysis of the all steels was undertaken using OM and SEM. The X80 steels all exhibited similar microstructures through the thickness; hence, only X80-462 steel will be discussed in detail. Similarly, the X100 steels all had similar microstructures; hence, only X100-2A steel will be discussed in detail.

1. *OM and SEM analysis of X80-462*

OM images of the X80-462 microstructure were taken from the top surface (0) and centerline (0.5) and are shown in Figures 4(a) and (b), respectively. SEM images taken from the same sample locations are shown in Figures 5(a) and (b), respectively. The microstructure consists primarily of polygonal ferrite (PF) with some acicular ferrite (AF). Qualitatively, the grain size is coarser at the centerline than at the surface. The average grain size (plus standard deviation) measured from SEM images, using the linear intercept method, are 2.04 (0.42) μm at the top surface and 2.57 (0.30) μm at the centerline.

2. *OM and SEM analysis of X100-2A*

OM images of the microstructures from near the top surface (0) and at the centerline (0.5) for X100-2A steel are shown in Figure 6. The microstructure consists primarily of bainitic ferrite (BF) with some acicular ferrite (AF) in the centerline samples. SEM images taken at the same through-thickness locations (Figure 7) show similar microstructures to those in the OM micrographs.

D. *TEM Analysis of X80-462 and X100-2A*

TEM was used to analyze both X80-462 and X100-2A steels at a position near the top surface (0). Figure 8(a) is a bright field image of X80-462 steel showing a complex microstructure consisting primarily of equiaxed grains as well as subgrains and an internal non-uniform dislocation network. The linear intercept method was applied to four different TEM images from X80-462 steel, encompassing 63 subgrains in total. The intercept length ranged from 216 to 704 nm with an average value of 500 nm and a standard deviation of 207 nm.

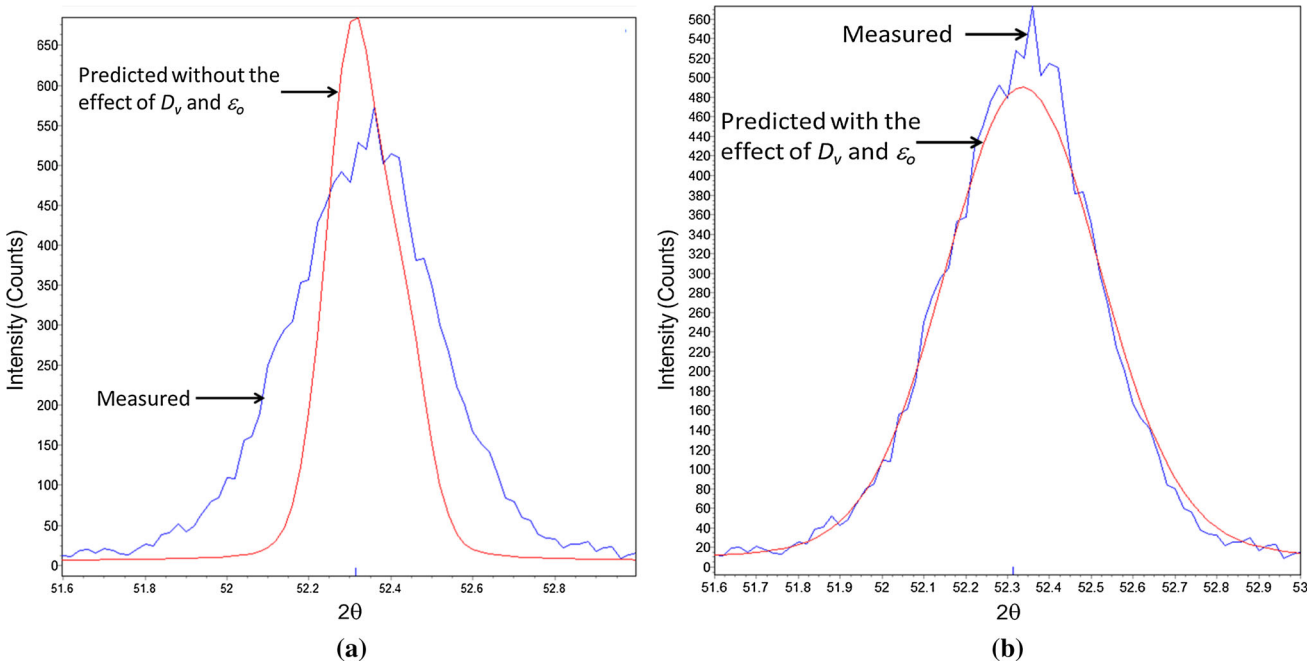

Fig. 3—Comparison of measured and calculated XRD patterns for the (110) peak of X100-2A steel (0.5): (*a*) without D_v and ε_o and (*b*) with the inclusion of D_v and ε_o.

Table II. QXRD Microstructure Values for X80 Steels

Relative Position*	D_v (nm)	ε_o (pct)	J	R_{wp}	(I_{110}/I_{211})	ΔFWHM (Deg)
X80-462						
0	4500	7.0	1.05	12.3	14.9	0.037
0.1	4500	6.1	1.03	11.9	13.0	0.038
0.5	4500	5.0	1.03	13.4	1.8	0.020
0.7	4500	5.7	1.09	13.3	1.3	0.027
1.0	136	5.8	1.05	12.1	2.1	0.093
X80-A4B						
0	223	7.5	1.05	11.2	18.2	0.041
0.3	4500	7.9	1.09	11.8	19.2	0.030
0.5	4500	7.8	1.17	13.6	0.8	0.051
0.8	103	7.2	1.11	13.7	1.9	0.055
1.0	99.8	7.1	1.16	10.6	24.4	0.061
X80-A4F						
0	104	7.3	1.02	16.4	10.6	0.067
0.3	61	6.4	1.21	12.3	0.5	0.087
0.5	50	6.1	1.26	11.9	0.2	0.077
0.8	4500	8.2	1.01	16.1	8.1	0.063
1.0	4500	5.6	1.09	13.1	11.6	0.043
X80-B4F						
0	4500	6.8	1.01	12.1	9.6	0.038
0.4	166	6.8	1.21	12.4	0.6	0.050
0.5	223	8.3	1.26	13.4	0.3	0.062
0.8	4500	6.6	1.11	13.0	2.1	0.039
1.0	4500	7.2	1.01	14.6	9.6	0.044

*0 corresponds to the top surface and 1.0 corresponds to the bottom surface of the pipe.

Figure 8(b) is a bright field image of X100-2A steel which exhibits a distinctive lath structure consistent with a bainitic ferrite (BF) morphology. Direct measurement (along the arrow) of individual lath thicknesses gave values ranging from ≈ 80 to 400 nm. As with the X80-462 steel, an internal non-uniform dislocation structure is present.

Table III. QXRD Microstructure Values for the X100 Steels

Relative Position*	D_v (nm)	ε_o (Pct)	J	R_{wp}	(I_{110}/I_{211})	ΔFWHM (Deg)
X100-2A						
0	69	11.5	1.12	19.5	21.7	0.244
0.3	82	15.4	1.11	19.8	3.4	0.300
0.5	40	12.6	1.27	23.6	0.4	0.177
0.7	4500	15.3	1.14	21.8	2.7	0.152
1.0	4500	12.8	1.12	18.4	22.7	0.135
X100-2B						
0	95	13.6	1.01	16.9	15	0.256
0.3	52	12.8	1.17	19.2	7	0.288
0.5	52	11.8	1.33	20.1	1	0.242
0.7	100	15	1.02	20.2	13	0.305
1.0	72	15.2	1.09	18.3	30	0.263
X100-3C						
0	74	12	1.12	12.1	20.8	0.134
0.3	223	13.7	1.03	12.0	13.0	0.188
0.5	52	11.2	1.29	13.3	0.4	0.180
0.7	81	10.6	1.30	13.4	0.2	0.115
1.0	100	12.7	1.03	13.6	4.5	0.136

*0 corresponds to the top surface and 1.0 corresponds to the bottom surface of the skelp.

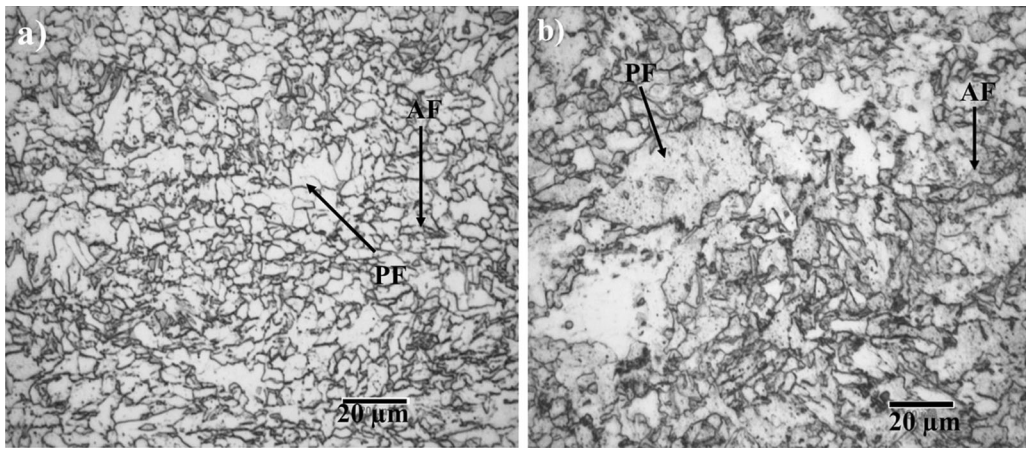

Fig. 4—OM images of X80-462 steel (*a*) near the top surface (0) and (*b*) at the centerline (0.5).

E. *EBSD Analysis of X80-462*

EBSD was used to analyze the microstructure at three positions (top surface (0), centerline (0.5), and bottom surface (1.0) of the pipe) through the thickness of X80-462 steel. Figure 9 is the EBSD map obtained from the 0 position. The red and pink lines represent high-angle grain boundaries (> 15 deg misorientation), the blue lines represent a misorientation of 5 to 15 deg, the yellow lines represent a misorientation of 2 to 5 deg, and the green lines represent a misorientation of 1 to 2 deg.

A mean linear intercept method was used to determine the subgrain size for each EBSD image. An area of 20 μm^2 was sampled and 20 random lines were drawn. The number of boundaries intercepted by each line was counted. The subgrain size was measured for all boundaries with a misorientation greater than 1 deg. Table IV summarizes the subgrain size at the three different locations through the thickness. Both the top (0) and bottom (1.0) surfaces exhibit finer subgrains than the centerline. The measured average subgrain size (388 nm) for the top surface is smaller than the average grain size directly measured from the TEM image (500 nm).

V. DISCUSSION

The QXRD results (Tables II and III) were examined to determine both the sensitivity and validity of QXRD in quantifying the microstructure for X80 and X100 steels. The effect of composition and processing (CIT, FRT) on crystallite size, J index, and microstrain was analyzed. The relation between the QXRD parameters and the measured yield stress and the Y/TS ratio was examined.

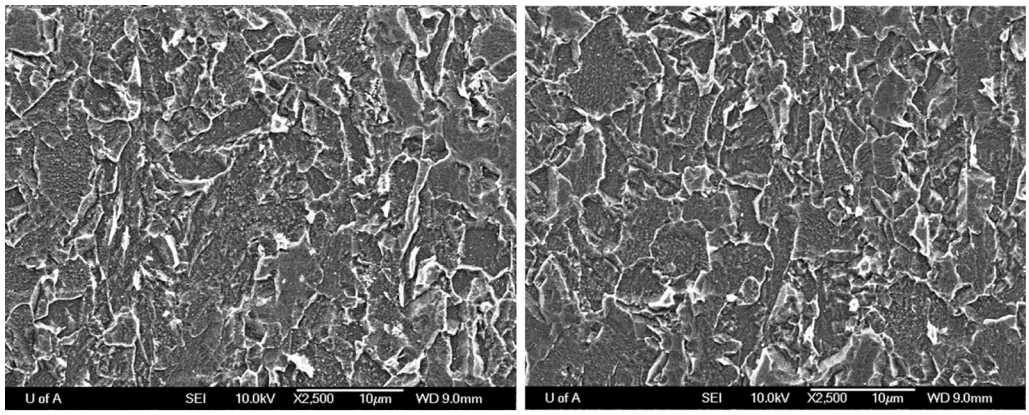

Fig. 5—SEM secondary electron (SE) images of X80-462 steel (*a*) near the top surface (0) and (*b*) at the centerline (0.5).

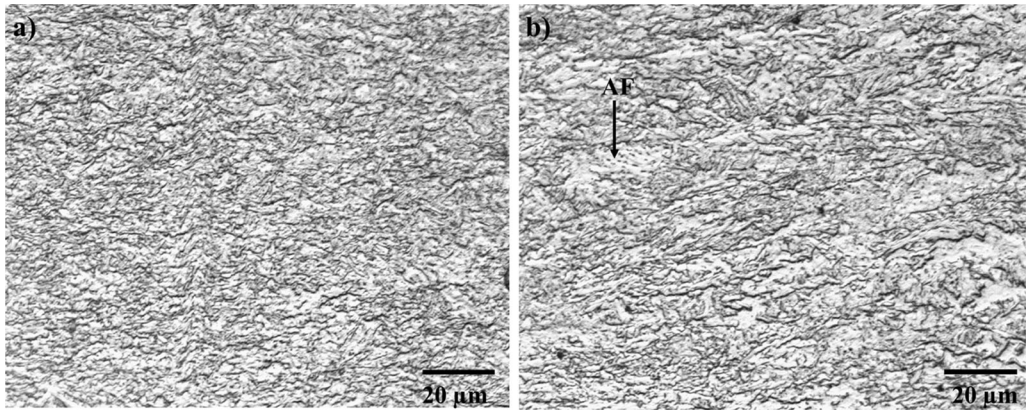

Fig. 6—OM images of X100-2A steel (*a*) near the top surface (0) and (*b*) at the centerline (0.5).

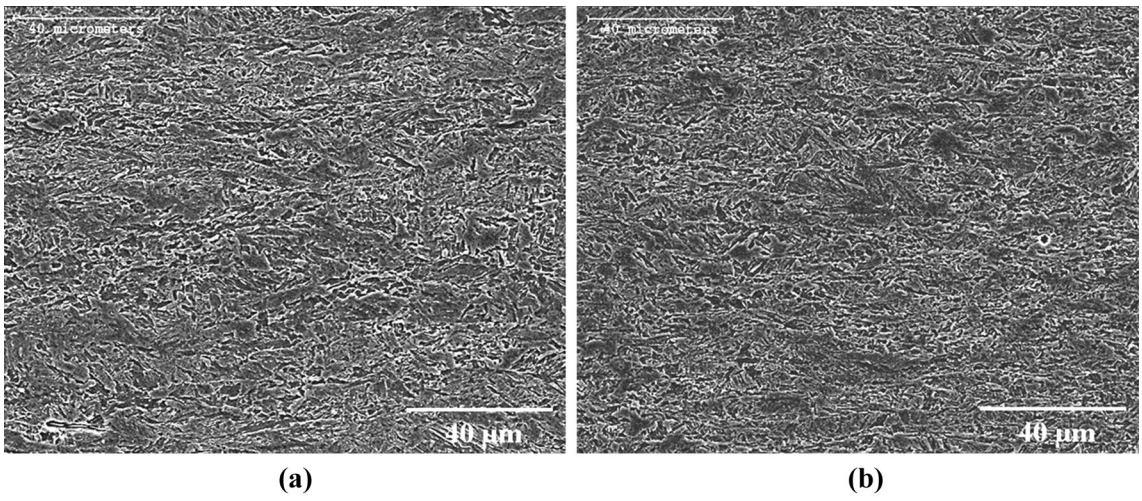

Fig. 7—SEM images of X100-2A steel (*a*) near the top surface (0) and (*b*) at the centerline (0.5).

A. *X80—ΔFWHM, TEM, and EBSD Analysis and Predicted Crystallite Size*

Table II shows a predicted D_v value of 4500 nm for eleven (11) of the twenty (20) X80 samples examined in this work. The value of 4500 nm is the default value of the whole profile fitting calculation when a crystallite size cannot be determined (*i.e.*, broadening of the diffraction peaks was insufficient to discern crystallite broadening). The value of microstrain predicted for these eleven X80 samples is between 5.0 and 8.2 pct.

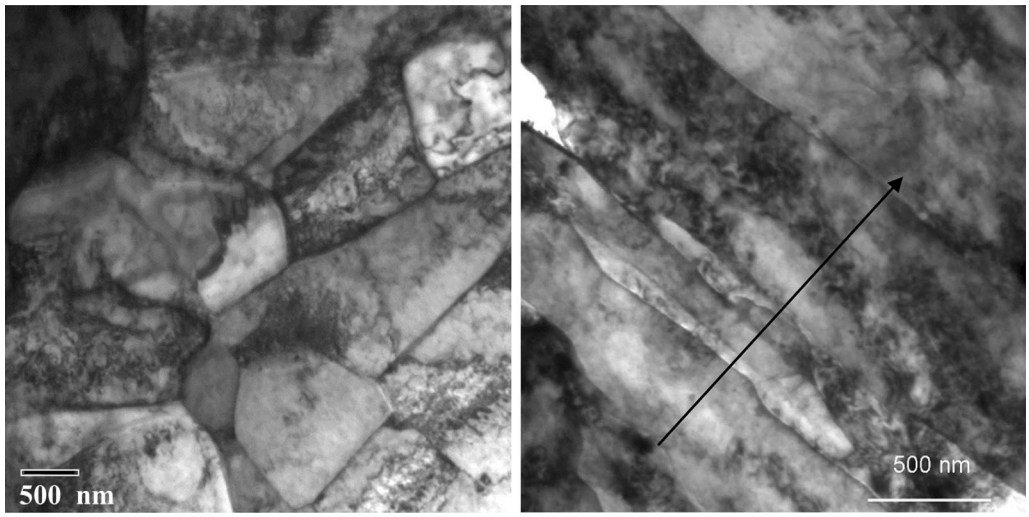

Fig. 8—TEM bright field images of (*a*) X80-462 steel (0) and (*b*) X100-2A steel (0).

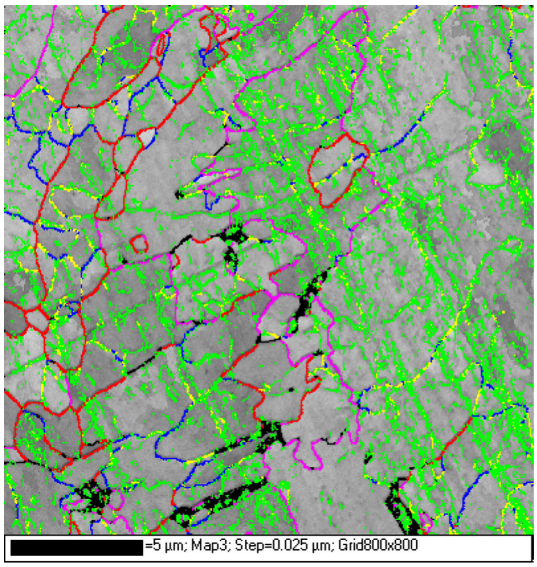

Fig. 9—EBSD map for X80-462 steel (0).

To determine the minimum amount of diffraction peak broadening necessary to provide meaningful crystallite size values for the X80 steels studied, a plot of $1/D_v$. *vs* ΔFWHM for the (110) diffraction plane is shown in Figure 10. The horizontal line in Figure 10 corresponds to a crystallite size of 223 nm (223 nm is the maximum reasonable value recorded for crystallite size in Tables II and III). At values of ΔFWHM < 0.050 deg (vertical line in Figure 10), a crystallite size could not be determined for ten samples. These data indicate that for the X80 steels studied in this work, the microstructural feature analogous to crystallite size are at the detection limit of the QXRD analysis.

The TEM bright field image for X80-462 from near the top surface (Figure 8(a)) qualitatively confirms that many of the grain/subgrain features in the X80 steels are larger than 223 nm. The grain size measured from four TEM images of X80-462 (0) resulted in a mean grain size of 500 nm with a standard deviation of 207 nm. The maximum grain size observed was 704 nm and the minimum size was 216 nm.

The subgrain (using a misorientation of ≥ 1 deg) size determined from EBSD analysis (Table IV) for the X80-462 steel was 319 to 475 nm for the top surface (0), 456 to 582 nm at the centerline (0.5), and 262 to 377 nm for the bottom surface (1.0). The larger subgrain size measured at the centerline of the sample is not surprising given the slower cooling rate (during laminar cooling) experienced at this location relative to the top and bottom surfaces. For both direct TEM and EBSD grain size measurements, the mean grain size is greater that the approximate detectable limit for QXRD of 223 nm.

For X80-462, a crystallite size could not be determined for either the top surface or the centerline. Both through-thickness positions had EBSD subgrain sizes significantly larger than the maximum detectable value (≈ 223 nm). However, the predicted D_v value for the bottom surface of X80-462 steel (1.0) (Table II) was 136 nm. Although the measured EBSD subgrain size is smaller at this steel position, it is still above the upper detectable size limit. This paradox between the EBSD measured subgrain sizes and the D_v value of 136 nm can be attributed to the misorientation limit of 1 deg used in the EBSD analysis. It is possible that the QXRD crystallite size broadening is sensitive to grain/subgrain misorientations ≤ 1 deg. As stated in the background section, the measured EBSD subgrain size (130 nm) for highly deformed copper[23] was more than double the predicted D_v value (63 nm).

Table IV. Subgrain Sizes (Average Intercept Length) for X80-462 Steel from EBSD Measurements

Normalized Position	Subgrain Size (nm)	SD (nm)	Range (nm)
0	388	41	319 to 475
0.5	471	30	456 to 582
1.0	324	32	262 to 377

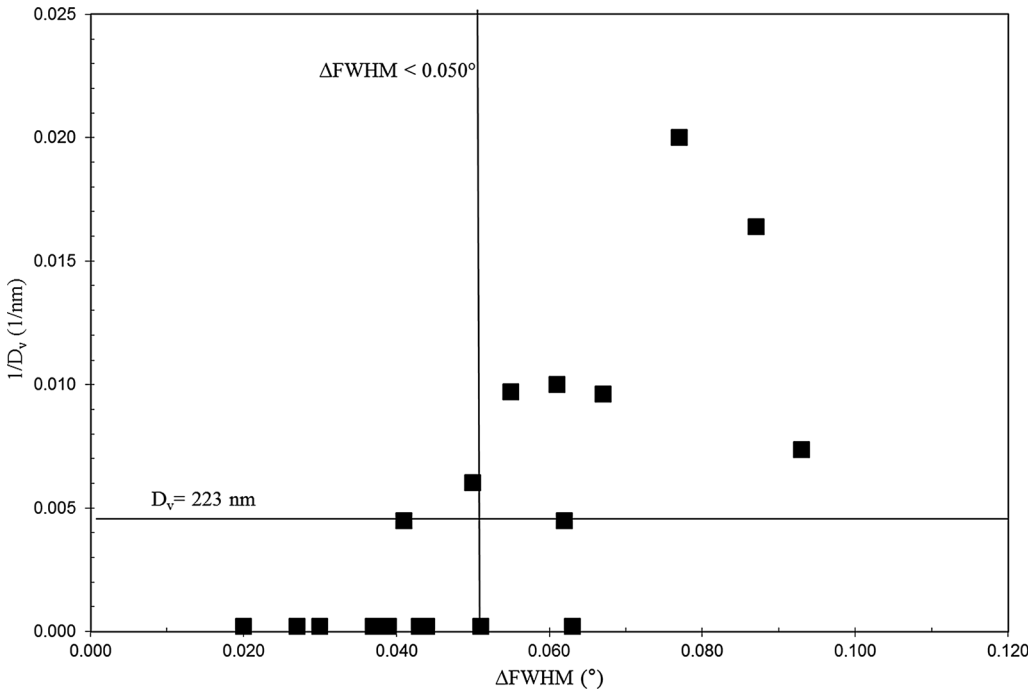

Fig. 10—$1/D_v$ *vs* ΔFWHM for the (110) diffraction peak for all X80 steels.

B. *X100—ΔFWHM, TEM, and Their Relation to Predicted Crystallite Size*

The X100 steels (Table III) all exhibited a ΔFWHM significantly greater than 0.050 deg (0.115 to 0.305 deg). Except for the steel samples X100-2A (0.7) and X100-2A (1.0), the value of the predicted crystallite size (D_v) for all the X100 samples was less than or equal to 223 nm. The TEM bright field image for X100-2A (0) (ΔFWHM = 0.244 deg) shown in Figure 8(b) exhibits grain/subgrain features both above and below 223 nm. The presence of the relatively thin laths (approximately 80 nm) associated with the bainite phase in these steels corroborate the QXRD predictions for the presence of fine crystallites (D_v = 69 nm). These results indicate that X100 microalloyed steels have a sufficiently fine microstructure (due to the presence of bainite) to be amenable to QXRD crystallite size microstructure analysis.

C. *Effect of Processing and Composition on Crystallite Size, Microstrain, and J index*

This section will analyze the correlation between the predicted QXRD microstructure parameters (*i.e.*, crystallite size, microstrain, and *J* index) and the processing parameters associated with each steel (CIT, FRT, and alloy content). Since FRT, alloy content (wt pct Ni + Mn + Mo) and CIT will simultaneously influence microstructure development (*i.e.*, the austenite to ferrite transformation) during laminar cooling, a combined parameter (pct AlloyFRT/CIT) that includes all these terms is used.

The ratio FRT/CIT is an indication of the cooling rate the steel undergoes when transforming from austenite to ferrite in the runout table. For similar laminar cooling configurations, a high FRT value and a low CIT value indicates a relatively high cooling rate. Qualitatively, a higher cooling rate (on the CCT curve for a microalloyed steel) will result in the formation of a predominantly acicular/bainitic ferrite structure *vs* a lower cooling rate where polygonal ferrite, and possibly pearlite, would be the predominant phases formed on austenite decomposition.

Similarly, increasing the alloying content (pct Alloy) will have the effect of shifting the CCT curve of the microalloyed steel to the right and is analogous to an increase in the cooling rate. Thus, both the FRT/CIT ratio and pct Alloy value will act in a similar manner (but of unknown magnitude) in terms of the phases formed during the austenite to ferrite transformation.

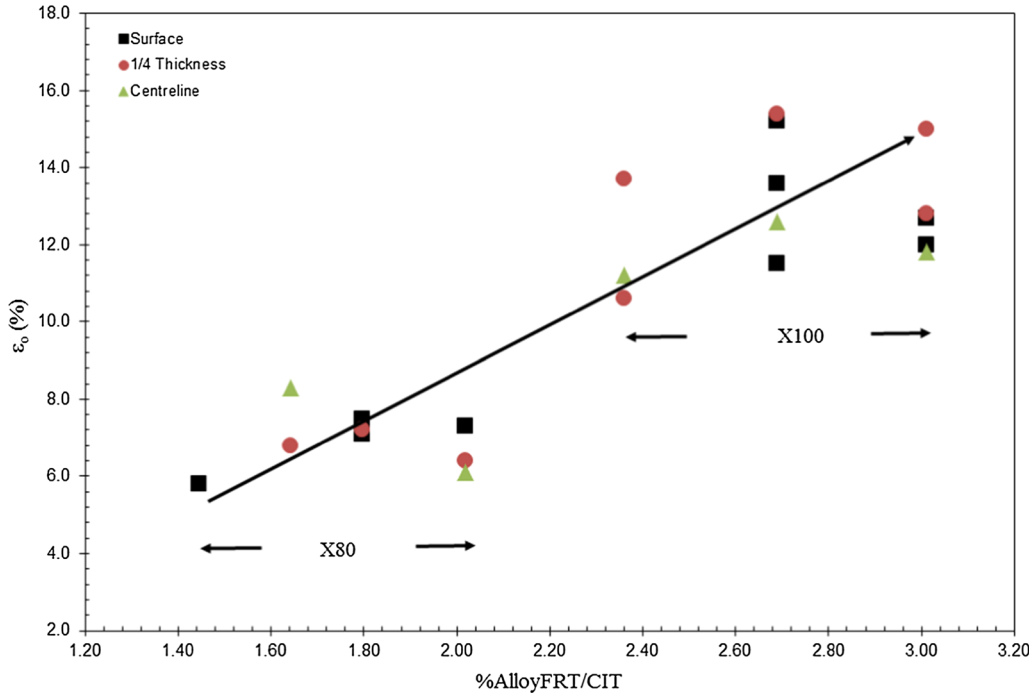

Fig. 11—ε_o *vs* pct AlloyFRT/CIT for X80 and X100 steels.

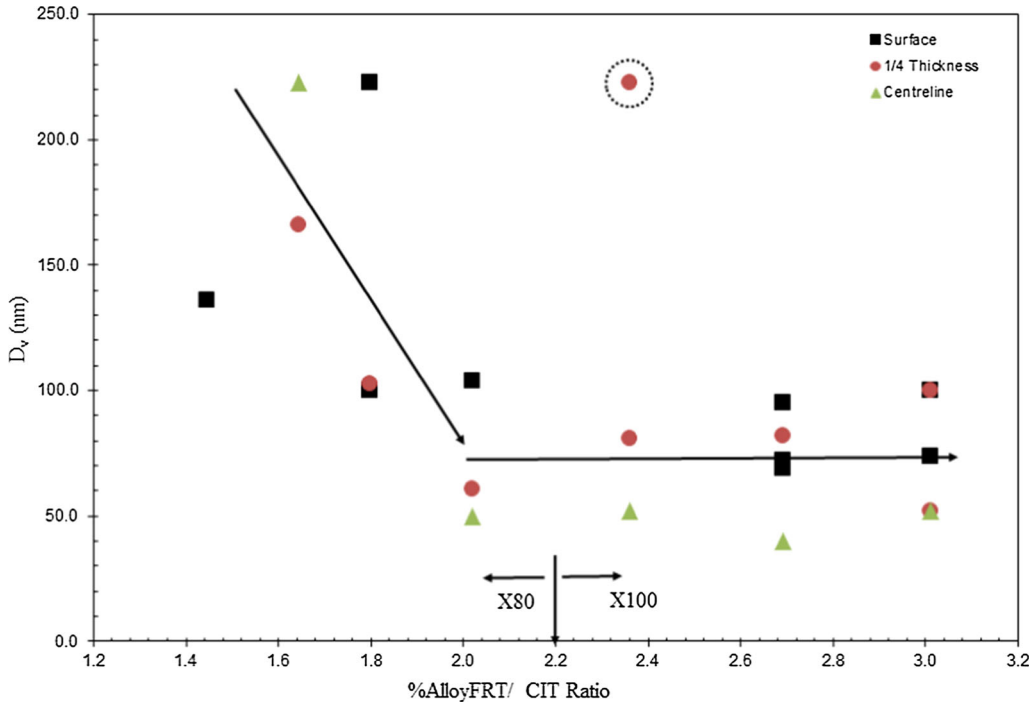

Fig. 12—D_v *vs* pct AlloyFRT/CIT for X80 and X100 steels.

1. *Effect of pct AlloyFRT/CIT on microstrain*

Figure 11 plots the microstrain (ε_o) as a function of the ratio of pct Alloy multiplied by FRT over the CIT (pct AlloyFRT/CIT). The data are limited to crystallite sizes ≤ 223 nm. The predicted value of microstrain is observed to increase with increasing pct AlloyFRT/CIT. This increase in microstrain is associated with the formation of predominantly bainitic ferrite that occurs at lower CIT values and/or higher alloying contents in the X100 steels. Higher dislocation densities are typically associated with bainitic ferrite that translates into a higher measured microstrain.

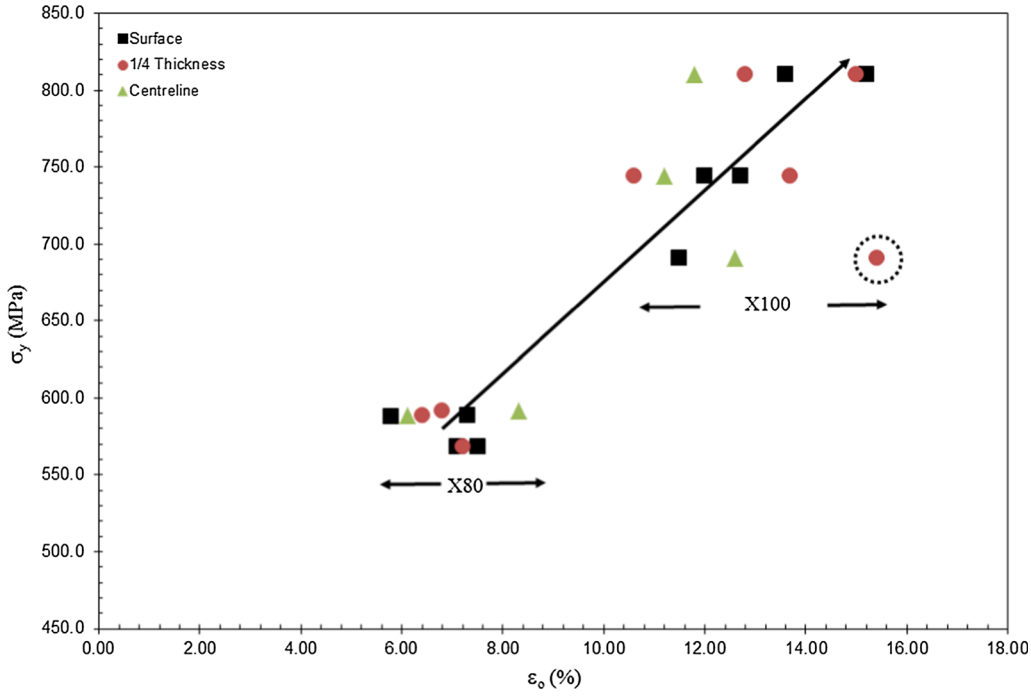

Fig. 13—Measured σ_y *vs* ε_o for both X80 and X100 steels.

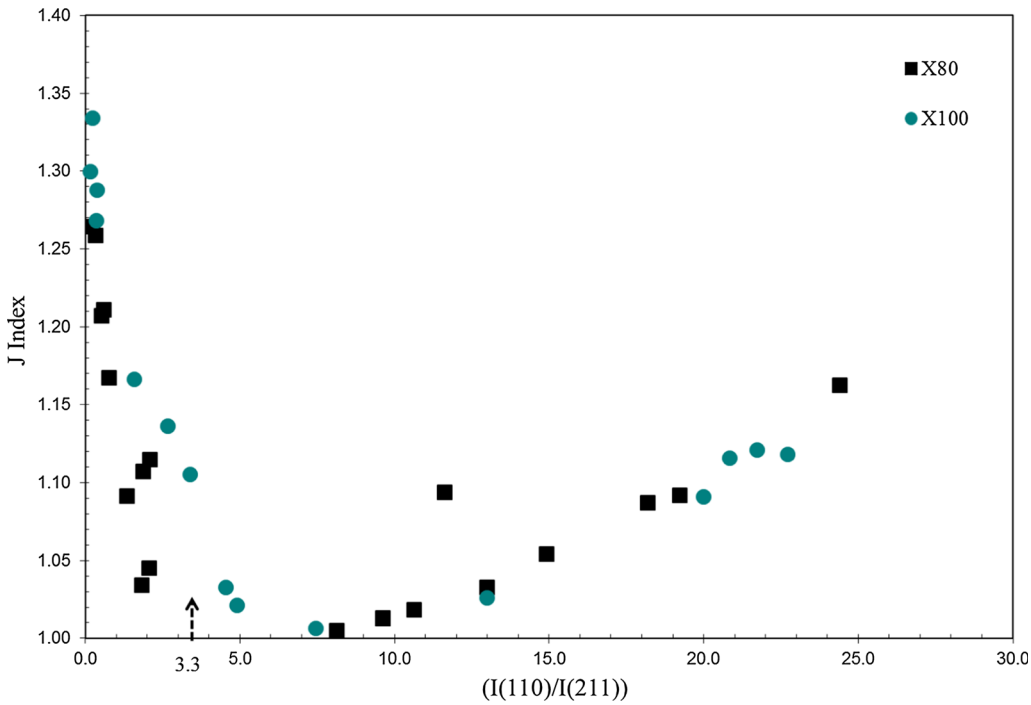

Fig. 14—*J* index *vs* ($I_{(110)}/I_{(211)}$) for all X80 and X100 steels and positions.

2. *Effect of pct AlloyFRT/CIT on crystallite size*

Figure 12 plots the crystallite size (D_v) as a function of the pct AlloyFRT/CIT. Unlike microstrain, the crystallite size is relatively constant except at lower pct AlloyFRT/CIT values (*i.e.*, low alloy content and high CIT) where an increase in crystallite size occurs with decreasing pct AlloyFRT/CIT. The transition from an entirely reconstructive transformation (*i.e.*, polygonal ferrite) at lower values of pct AlloyFRT/CIT to a displacive transformation (bainitic ferrite) at higher values of pct AlloyFRT/CIT may account for the differences in measured crystallite size. This later phase

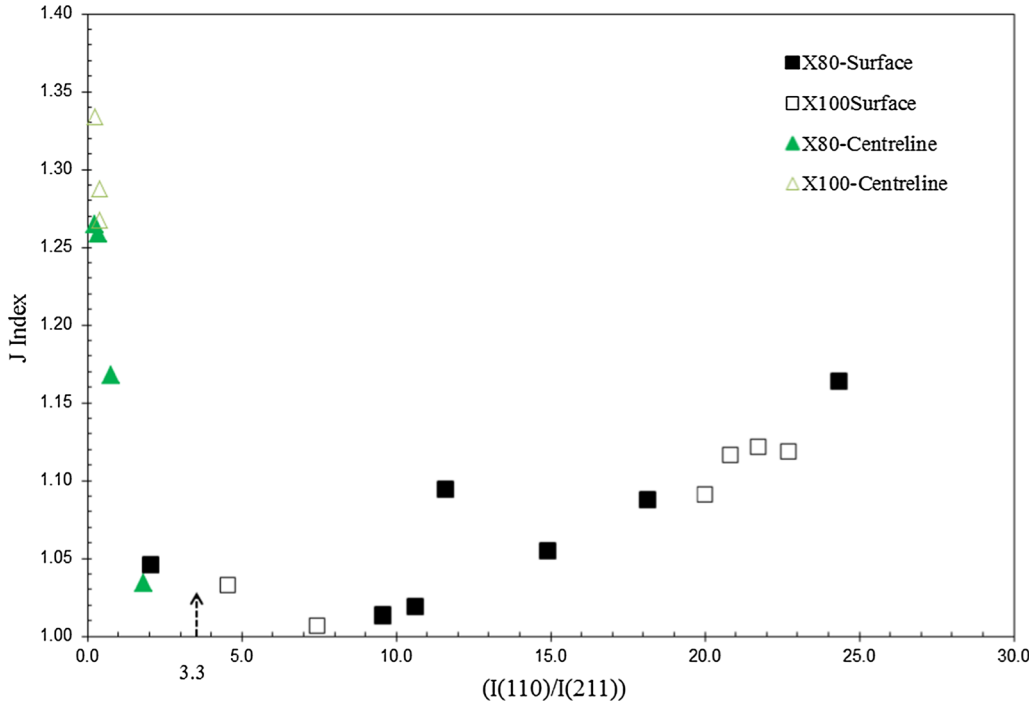

Fig. 15—*J* index *vs* ($I_{(110)}/I_{(211)}$) at the centerline and surface for X80 and X100 steels.

is the predominant phase observed in the X100 steel (Figures 6, 7 and 8(b)). The crystallite size for pct AlloyFRT/CIT greater than 2.0 becomes independent of pct AlloyFRT/CIT suggesting that the bainitic ferrite formed at these levels of pct AlloyFRT/CIT are comparable to each other. The circled data point for X100-3C at the ¼ thickness is considered an outlier.

3. *Effect of pct AlloyFRT/CIT on J index*

The relationship between the *J* index value and pct AlloyFRT/CIT was explored. A correlation was not observed. This suggests that the main processing factors affecting the *J* index are the rough and finish rolling conditions and not the laminar cooling conditions (*i.e.*, FRT and CIT).

D. *Effect of Microstrain and Crystallite Size on Mechanical Properties*

This section analyzes the correlation between the QXRD predicted microstrain and crystallite size and the measured bulk yield strength (σ_y). For the purpose of this work, microstrain is proportional to the square root of the dislocation density[31] and the crystallite size is considered analogous to grain size.

1. *Effect of microstrain on yield stress*

Figure 13 is a plot of σ_y *vs* ε_o for both the X80 and X100 steels. The data are clustered into two distinct groups corresponding to the X80 steels at low yield strength values and the X100 steels at higher strength values. The yield stress is observed to increase with increasing microstrain (the data point circled in the graph is considered an outlier). The higher yield strengths for the X100 steels (relative to the X80 steels) can thus be partially attributed to a higher microstrain (*i.e.*, higher dislocation density) associated with the bainitic ferrite microstructure.

2. *Effect of crystallite size on yield stress*

The yield stress does not show any correlation with measured crystallite size for both the X80 and X100 steels. This lack of correlation suggests that crystallite size is a measure of the size of low-angle subgrains (present in both X80 and X100) that does not contribute significantly to yield strength.[32] The similarity between the measured EBSD grain size data for X80-462 (1.0) shown in Table IV (262 to 367 nm) for a grain boundary angles > 1.0 deg and the crystallite size determined for this location (136 nm) supports this postulation.

3. *Effect of microstrain and crystallite size on the Y/T ratio*

A correlation between Y/TS and ε_o is similar to that observed for σ_y *vs* ε_o (Figure 13). This similarity is attributed to the dominance of yield stress in the measured Y/T ratios. In an analogous manner, the Y/T ratio did not show any correlation with the crystallite size.

E. *J Index Variation with Through-Thickness Position*

As discussed earlier, the *J* index quantifies the magnitude of preferred orientation but does not provide information on the predominant texture variants. For the purpose of this work, both the *J* index from QXRD

and the ratio of XRD intensities for the (110) and (221) peaks ($I_{(110)}/I_{(211)}$) from the diffraction patterns will be discussed. The (110) and (211) planes are both relevant texture variants that can occur in TMCP steels.[33,34]

Figure 14 is a graph of the J index plotted as a function of the ($I_{(110)}/I_{(211)}$) ratio for both the X80 and X100 steels at all through-thickness positions. The ($I_{(110)}/I_{(211)}$) ratio for a completely random (*i.e.*, non-textured) XRD pattern is 3.3 (*i.e.*, (100/30)). This value has been marked in Figure 14. There are two groupings in Figure 14, corresponding to $(I_{(110)}/I_{(211)}) > 3.3$ and $(I_{(110)}/I_{(211)}) < 3.3$—both of which have the same J index. This indicates that although the QXRD J index can have a similar value the underlying texture variant can be significantly different. Both X80 and X100 steels have J index values in the two groupings.

Figure 15 is a graph of the texture index J *vs* the ($I_{(110)}/I_{(211)}$) ratio for the centerline and surface samples for both X80 and X100. The surface and centerline samples clearly exhibit completely different texture variants. In the former, the ($I_{(110)}/I_{(211)}$) ratio is greater than 3.3 (except for one data point), while the centerline samples always exhibit $I_{(110)}/I_{(211)} < 3.3$ even when the J index values are the same. The texture index J and the ($I_{(110)}/I_{(211)}$) ratio values at the ¼ thickness position show ($I_{(110)}/I_{(211)}$) ratios both above and below 3.3.

The presence of a variation in the intensity of either plane is not surprising as both are relevant texture components in hot-rolled steel.[33,34] The through-thickness texture variation is attributed to a difference in deformation state at the centerline *vs* the near-surface location.[35] The similarity among the X80 and X100 steel textures may be a partial consequence of similar finish rolling temperatures (FRT)[35] and hot rolling schedules. The larger J index at the centerline indicates a higher degree of preferred orientation exists at this position. However, given the complexity of texture[36] that can occur during transformation of deformed austenite to ferrite, it is difficult to draw further conclusions on the relation between the J index and the $(I_{(110)}/I_{(211)})^{1/2}$ ratio.

VI. CONCLUSION

The following microstructure and mechanical property conclusions are drawn from the through-thickness quantitative X-ray diffraction (QXRD) characterization of X80 and X100 microalloyed pipeline steels.

1. QXRD crystallite sizes were measured for both the X80 and X100 steels; however, an upper detection limit for crystallite size of ≈ 223 nm was observed. The crystallite sizes measured by QXRD for the X80 steels studied were both above and below this detection limit. EBSD grain size analysis of the X80 confirmed the presence of subgrains near this detection limit. The crystallite sizes measured for the X100 steels were predominantly finer than 223 nm and were typically in the 40 to 100 nm range. TEM analysis confirmed the presence of microstructural features on this scale.
2. The measured QXRD microstrain was higher (11.5 to 15.3 pct) for the X100 steels relative to the X80 steels (5.0 to 8.3 pct). The microstrain increased with decreasing cooling interrupt temperature (CIT) and increasing alloy content. This difference is associated with a change in the microstructure from ferritic/acicular ferrite to predominantly bainitic ferrite.
3. The yield strength of the steels was independent of the measured crystallite size but increased with increasing microstrain. A similar correlation between the yield-to-tensile strength ratio (Y/TS) was observed with microstrain indicating the predominance of the yield stress in the Y/T ratio value.
4. The severity of crystallographic texture, as quantified by the J index value, was similar for both the X80 and X100 steels. The largest J index values for both X80 and X100 were observed at the centerline of the steel.
5. QXRD has been shown to provide microstructural information, *e.g.*, trends in grain/subgrain size and microstrain development, for several microalloyed steels. This information can be correlated to steel composition and processing conditions and for the microstrain measurements, can be related to yield strength.

ACKNOWLEDGMENTS

The authors would like to thank the Natural Sciences and Engineering Research Council (NSERC) of Canada, EVRAZ N.A., Enbridge, TransCanada Pipelines, Alliance Pipelines and UT Quality for financial assistance. The authors would also like to thank Laurie Collins for his insight and continued support of this work.

FUNDING

This work was supported by NSERC (CRDPJ 418942 – 11).

REFERENCES

1. J. Lu: PhD Thesis, University of Alberta, 2009.
2. X. Li: M.A. Sci. Thesis, University of Alberta, 2009.
3. W. Wang, W. Yan, L. Zhu, P. Hu, Y. Shan, and K. Yang: *Mater. Des.*, 2009, vol. 30, pp. 3436–43.
4. W. Wang, Y. Shana, and K. Yanga: *Mater. Sci. Eng. A*, 2009, vol. 502, pp. 38–44.
5. S. Shanmugama, R.D.K. Misra, J. Hartmann, and S.G. Jansto: *Mater. Sci. Eng. A*, 2006, vol. 441, pp. 215–29.
6. S. Shanmugama, N.K. Ramisetti, R.D.K. Misra, J. Hartmann, and S.G. Jansto: *Mater. Sci. Eng. A*, 2008, vol. 478, pp. 26–37.
7. K. Junhua, Z. Lin, G. Bin, L. Pinghe, W. Aihua, and X. Changsheng: *Mater. Des.*, 2004, vol. 25, pp. 723–28.
8. Z. Tang and W. Stumpf: *Mater. Char.*, 2008, vol. 59, pp. 717–28.
9. M. Diaz-Funetes, A. Iza-Mendia, and I. Guitierrez: *Metall. Trans. A*, 2003, vol. 34A, pp. 2505–16.
10. R.K. Ray, M.P. Butron-Guillejni, and J. Jonas: *ISIJ Int.*, 1992, vol. 32 (2), pp. 203–12.

11. P. Cizek, B.P. Wynne, C.H.J. Davies, B.C. Muddle, and P.D. Hodgson: *Metall. Trans. A*, 2002, vol. 33A, pp. 1331–49.
12. I.A. Yakubtsov, P. Poruks, and J.D. Boyd: *Mater. Sci. Eng. A*, 2008, vol. 480, pp. 109–16.
13. M.C. Zhao, K. Yang, F. Xiao, and Y.Y. Shan: *Mater. Sci. Eng. A*, 2003, vol. 355, pp. 126–36.
14. D. Bhattacharjee, J.F. Knott, and C.L. Davies: *Metall. Trans. A*, 2004, vol. 35A, pp. 121–30.
15. J.B. Wiskel, J. Lu, O. Omotoso, D.G. Ivey, and H. Henein: *Metals*, 2016, vol. 6, p. 90.
16. J.I. Langfordy and D. Louer: *Rep. Prog. Phys.*, 1996, vol. 59, pp. 131–234.
17. R.A. Young: *The Rietveld Method*. R.A. Young, ed., Oxford University Press: Oxford, 1993, pp. 1–30.
18. R. Kuzel, V. Holy, M. Cernansk, J. Kubena, D. Simek, and J. Kub: *Diffraction Analysis of the Microstructure of Material*. E.J. Mittemeijer, and P. Scardi, eds., Springer, New York, 1984, pp. 229–45.
19. A.A. Coelho: Topas Academic version 4.1, 2007.
20. P. Scardi and M. Leoni: *Diffraction Analysis of the Microstructure of Material*. E.J. Mittemeijer and P. Scardi, eds., Springer, New York, 1984, pp. 51–91.
21. D. Chakrabarti, M. Strangwood, and C. Davis: *Metall. Trans. A*, 2009, vol. 40A, pp. 780–94.
22. K. Poorhaydari and D.G. Ivey: *Mater. Char.*, 2007, vol. 58, pp. 544–54.
23. F. Dalla Torre, A. Gazder, C.F. Gu, C.H.J. Davies and E.V. Pereloma: *Metall. Trans. A*, 2007, vol. 38A, pp. 1080–95.
24. F. Dalla Torre, P. Spatig, R. Schaublin, and M. Victoria: *Acta Mater.*, 2005, vol. 53, pp. 2337–49.
25. P. Sahu: *J. Appl. Cryst.*, 2005, vol. 38, pp. 112–20.
26. D. Martinez-Blanco, P. Gorria, J.A. Blanco, M.J. Perez, and J. Campo: *J. Phys. Condens. Mater.*, 2008, vol. 2, pp. 1–10.
27. S. Murugesan, P. Kuppusami, E. Mohandas, and M. Vijayalakshmi: *Mater. Lett.*, 2012, vol. 67, pp. 173–76.
28. C.C. Tang, P.A. Lynch, R.W. Cheary, and S.M. Clark: *J. Appl. Cryst.*, 2007, vol. 40, pp. 642–49.
29. R.A. Renzetti, H.R.Z. Sandim, R.E. Bolmaro, P.A. Suzuki, and A. Moslang: *Mater. Sci. Eng. A*, 2012, vol. 534, pp. 142–46.
30. R.B. Von Dreele: *J. Appl. Cryst.*, 1997, vol. 30, pp. 517–25.
31. J. Han, C. Ju, B. Wu, J. Li, H. Li, Y. Lu, and Q. Gao: *Mater. Sci. Eng. A*, 2017, vol. 683, pp. 123–28.
32. N. Hansen: *Scripta Mater.*, 2004, vol. 51, pp. 801–06.
33. P Juntunen, D Raabe, P Karjalainen, T Kopio, and G Bolle: *Metall. Mater. Trans. A*, 2001, vol. 32A, pp. 1989–95.
34. R.K. Ray, J.J. Jonas, M.P. Butron-Guillen, and J. Savoie: *ISIJ Int.*, 1994, vol. 34 (12), pp. 927–42.
35. Y.B. Park, D.N. Lee, and G. Gottstein: *Acta Mater.*, 1996, vol. 44 (8), pp. 3421–27.
36. J.J. Jonas: *Proc. Int. Conf. Microstructure and Texture in Steels and Other Materials*, Jamshedpur, India 2008, Feb 5–7, pp. 3–16.
37. C. Mapelli, R. Venturini and R. Riva: La Revue de Metalurgie CIT, 2007, pp. 98–105.